Thermodynamic Modelling and Real-Time Control Strategies of Solar Micro Gas Turbine System with Thermochemical Energy Storage

Jiamin Yang[1], Gang Xiao[1*], Mohsen Ghavami[2], Jafar Al-Zaili[2], Tianfeng Yang[1], Abdulnaser Sayma[2], Dong Ni[3]

[1]State Key Laboratory of Clean Energy Utilization, Zhejiang University, Hangzhou, China

[2] City, University of London, London, United Kingdom

[3] College of Control Science and Engineering, Zhejiang University, Hangzhou, China

[*]Email: xiaogangtianmen@zju.edu.cn

Abstract

Distributed solar gas turbine systems with thermal energy storage are expected to overcome the intermittence and instability of solar irradiance and produce reliable and flexible electricity for remote districts and islands. Here, a mathematical model is developed for a 10 kW_e solar micro gas turbine (MGT) system with thermochemical energy storage (TCES) to study the system thermodynamic characteristics at real-world direct normal irradiation (DNI) variations. Real-time control strategies aiming for stable operation and set-point tracing are proposed and implemented in transient simulations to analyze the control effect against both short- and long-term DNI disturbances based on system dynamics. Results show that, by regulating the output power, rotational speed (N) is kept constant, and system responses are smoothened (e.g., less than 5.8% fluctuation of the mass flow rate). Power regulation also enables a constant turbine outlet temperature (TOT) and the optimal overall performance (e.g., output power and total efficiency exceeding 14 kW_e and 14%, respectively). By combining power and bypass regulations, N and TOT can simultaneously remain constant while outputting a stable power of 12.6 kW_e ± 5% under 750 ~ 820 W/m^2, with a sharp drop to 500 W/m^2. For favorable weather, N-TOT simultaneous control can guarantee the high and stable system performance. If massive clouds appear, constant TOT operation is more advantageous during peak load demand for larger electricity generation, while constant N operation is preferable during low power demand for smoother turbine operation.

Furthermore, the addition of TCES smoothens the performance variation and prolongs the generation duration. TCES also allows constant TOT operation to store up to 32% more energy than constant N and output 18 ~ 28 kWh more energy during daytime operation, thanks to the higher operating temperature. Overall, the proposed real-time control methods reduce the dependency on fossil fuel combustion and contribute to the stable, safe, and efficient operation of a distributed high-percentage-solar-share MGT system.

Keywords: Solar-MGT; thermochemical energy storage; thermodynamic model; control strategies

Highlights

- Control tactics are offered for high-percentage-solar-share MGT-TCES systems
- Real-time control is analyzed under both short- and long-term DNI disturbances
- N and TOT can be simultaneously controlled by power and bypass regulations
- TCES shows better compatibility with constant TOT operation than constant N

1 Introduction

Micro gas turbine (MGT) is a promising option for solar power plants due to the advantages of rapid response (Wacek and Ferguson), high reliability (Schwarzboezl et al., 2006), low water consumption (Quero et al., 2014; Schwarzboezl et al., 2006), and modest capital cost (Wacek and Ferguson) compared to traditional solar steam turbine systems. The compactness, operation stability and relatively high efficiency (Cohen et al., 1996) of MGT make it a competitive candidate for distributed energy systems. The addition of solar power also reduces fuel consumption and greenhouse gas emission in gas turbine generation systems. The early documented solarized MGT systems were hybrid-powered with natural gas or biomass fuel. The first MGT solarization project, Solar hybrid gas turbine electric power system (SOLGATE), started in 1998 with support by the European Commission (EC), and had reached 800℃ at the receiver outlet and outputted 230 kW_e with a ~ 60% solar share. An adapted control system and transient simulation models in TRNSYS software were also developed (European Commission, 2005; Heller et al., 2006; Sinai et al., 2005). Solar-Hybrid Power and Cogeneration Plants (SOLHYCO), regarded as an extension of SOLGATE as well as a step forward to commercialization, tried to optimize the pressurized air receiver and developed an MGT prototype for a solar-hybrid system (Amsbeck et al., 2008; Amsbeck et al., 2010; European Commission, 2011; Heller et al., 2009). Solar Up-scale Gas Turbine System (SOLUGAS) was the first MW-level demonstration project and generated 2.5 MWe during the test. It was kept running for over one year. SOLUGAS also accomplished accurate receiver efficiency evaluation and control optimization, including startup and shutdown processes (Korzynietz et al., 2016; Korzynietz et al., 2012; Quero et al., 2014). In 2010, Commonwealth Scientific and Industrial Research Organization (CSIRO) and Mitsubishi Heavy Industries (MHI) investigated a solar air turbine system's technical feasibility and studied the components and system performances through test and modeling, respectively. High-temperature thermal energy storage (TES) technology was also experimentally studied, though it was excluded from the final pilot-scale and commercial-scale systems due to its immaturity (CSIRO, 2014; Hiromi et al., 2012). AORA Solar commissioned two solar-hybrid co-generation plants outputting 100 kW_e and 170 kW_{th} in Kibbutz Samar, Israel (2009) and Plataforma Solar de Almería, Spain (2012), respectively (Ssebabi et al., 2019). In 2013, another EC funded project, Optimized Microturbine Solar Power system (OMSoP), attempted to develop a 5 kW_e MGT system purely driven by concentrated solar power (CSP). Thereupon, operation, and control strategies were proposed and analyzed (Ghavami et al., 2017; Lanchi et al., 2015).

Among these solar-only/solar-hybrid MGT projects, however, the potential of TES has barely been explored and is one of the obstacles against high-percentage-solar-share power generation. For CSP plants, the annual solar share is typically lower than the nominal value, leading to the inevitable wasted heat production when DNI approaches or exceeds the design value (Spelling and Laumert, 2014). Moreover, hybrid power such as supplementary combustion is necessary for a continuous generation due to the intermittent and unstable nature of solar irradiance (Schwarzboezl et al., 2006). The rapid increase in the amount and proportion of renewable electricity calls for the improvement of energy storage technology to ensure the stability and safety of the power grid in a region. Therefore, TES should be optimized to establish stabilized electricity production and reduce wasted heat to improve annual solar share while avoiding the construction of an oversized CSP plant (Spelling and Laumert, 2014). TES can also significantly reduce the levelized cost of energy (LCOE) (CSIRO, 2014) and CO_2 emissions when the flexibility of CSP plants are used to fulfill the demand for renewable electricity within the market (Guédez et al., 2013).

TES can operate as one of three different techniques, i.e., sensible heat, latent heat, and thermochemical energy. Sensible heat storage stores the thermal energy by increasing the temperature of

a storage medium, such as ceramic. It is currently the most mature TES technology (Tian and Zhao, 2013). Latent heat storage stores energy through the phase transition of materials, such as fatty acids, which allows higher energy storage density than sensible heat storage with lower heat transfer performance and the pressure change during the phase transition. The large-scale application of latent heat storage is currently under development (Xu et al., 2015; Zalba et al., 2003). Thermochemical energy storage (TCES) has a higher temperature range due to chemical reactions, including carbonation-decarbonization (Edwards and Materić, 2012), redox (Carrillo et al., 2014), decomposition/synthesis (Lovegrove et al., 2004), and hydration-dehydration (Criado et al., 2014). The energy density of TCES is 5 times and 1.6 times higher than sensible heat and latent heat storage, respectively (Fallahi et al., 2017; Tescari et al., 2015), which makes it suitable for compact arrangement and high-temperature utilization. However, the application technology is still under development. Among all TCES materials, metal oxides have good compatibility with air, and their equilibrium temperature range is well-suited to the working temperature of a high-temperature air receiver. Due to these reasons, the coupling of metal oxides into TES in CSP plants has recently drawn research interests (Singh et al., 2017; Tescari et al., 2014; Yang et al., 2017). By introducing metal-oxide-based TCES into the solar-MGT system, the incident solar energy can be redistributed according to user demand, allowing for the generation of continuous and steady electricity, even under harsh climate conditions or during nighttime. A TCES unit can also serve as a protection mechanism by stabilizing the inlet temperature of the turbine or combustor (Spelling et al., 2014). Nevertheless, the complicated thermochemical characteristics and the large thermal inertia of TCES add more complexity and uncertainty to the dynamic response and systematic control.

Dynamic simulations of solarized gas turbine with/without TES have been conducted to investigate the transient behaviors and form the control strategies. Over the past few decades, transient and dynamic models of the gas turbine system have been developed in Modelica (Haugwitz, 2003), FORTRAN (Henke et al., 2017), and MATLAB/Simulink (Traverso, 2004) software, amongst others, and have been verified with commercial MGTs. Merchán (Merchan et al., 2017) developed a thermodynamic model to explore the hybridization and configurations of a solar-hybrid gas turbine system using hourly solar irradiance input. Grange (Grange et al., 2016) built a pseudo-dynamic model and adopted different operation strategies to perform a typical-day analysis on a solar-hybrid gas turbine system with two receivers and a pack-bed TES unit. Traverso (Traverso et al., 2014) conducted a dynamic analysis in TRANSEO for a 12 MW_e solar-hybrid MGT system with sensible TES and proposed control strategies to stabilize output power and restrict TOT. Olivenza-León et al. (Olivenza-León et al., 2015) developed a thermodynamic model for a regenerative solar-hybrid gas turbine system without TES and validated the model with the SOLUGAS plant (Korzynietz et al., 2012), which has a commercial gas turbine, the Mercury 50. Bittanti (Bittanti et al., 2013) proposed the control strategies for a solarized gas turbine system and emulated the response under the step-change of fuel flow and solar irradiance. Wang (Wang et al., 2018) proposed four potential control methods for receivers in a solar dish gas turbine system to help prevent the absorber overheating, which was numerically discussed using the ray-tracing tool FRED® and the computational fluid dynamics software ANSYS Fluent®. More recently, Ssebabi et al. (Ssebabi et al., 2019) modeled both the steady-state and transient performance of a solar-hybrid MGT system consisting of the SOLGATE receiver (European Commission, 2005) and two turbines from commercial turbochargers, which generate hot gas and output power, respectively. The transient results obtained from the quasi-steady state calculation illustrated the fuel flow control effect under sudden irradiance change.

The majority of the solar-MGT studies focus on the hybrid systems, whose control system mainly depends on fuel flow regulation (European Commission, 2005; Fisher et al., 2004; Heller et al., 2006; Korzynietz et al., 2016; Llamas et al., 2019; Quero et al., 2014; Schwarzboezl et al., 2006; Ssebabi et al., 2019) by a fast-acting fuel control valve. Other popular safety control measures include blow-off valves, mechanical brakes, and shunt resistors loading the generator to avoid rotor overspeed and compressor surge (Buck et al., 2017). To increase the solar share and mitigate CO_2 emissions, new control methods that do not depend on fuel consumption need to be proposed and further improved. Rovense et al. (Amelio et al., 2018; Rovense, 2015; Rovense et al., 2016; Rovense et al., 2017) proposed a mass flow control method for a closed-loop unfired solar air Brayton cycle. By adding an auxiliary compressor and a bleed valve at the compressor entrance and the turbine exit, respectively, the main mass flow rate can be regulated to maintain constant TIT/system efficiency. Rovense et al. (Rovense et al., 2016) integrated a double-tank molten salt TES unit into a solar-only gas turbine system. The results showed that the integration increased the system capacity factor as well as the operation hours, while providing a promising LCOE. Efforts were also made to include a double-tank particle storage system into the unfired closed-loop solar air Brayton cycle (Rovense et al., 2019). With the mass flow regulation and heliostats defocusing systems as actuators, the system could follow the electricity demand curves for 59% to 68% time of the year. Ghavami et al. (Ghavami et al., 2017) proposed three control strategies for a dish-MGT system without TES: power regulation, recuperation control, and their combination, along with the power electronics realization as well as system thermodynamic analysis. Ellingwood et al. (Ellingwood et al., 2019) proposed a recycle control scheme to replace the heliostat field control when coping with excessive solar radiation. By recycling the exit flow of TES into receiver, the receiver outlet temperature was restricted within safe value. This control method improved the annual solar fraction and solar-to-electricity efficiency. It was further improved in (Ellingwood et al., 2018) where a TES on/off bypass mechanism was added to reduce charging rate and prolong recycling duration.

Despite the research efforts and achievements above, there remain several aspects to be further improved in solar gas turbine area:

(1) The potential of TES has yet to be fully exploited. The deeper penetration of solar energy calls for different control methods other than fuel combustion, and the popular solar component control method, i.e. heliostat defocusing, is not the best option which wastes the available solar power. The thermodynamic features of TES could play a more significant role in operation control.

(2) Little attention is paid on single-tank TES control. Although the double-tank molten salt TES technology is mature and generally employed in CSP plants (Achkari and Fadar, 2019), and the double-tank particle-based TES technology recently draws increasing attention in supercritical CO_2 Brayton cycle area, such as (Albrecht and Ho, 2017), the single-tank metal oxides TCES is a better match for solar gas turbine system. Unlike the double-tank configuration which is able to utilize the mass flow rate or flow direction of the storage medium, the degree of freedom is more limited in single-tank TCES control, and its influence on a CSP gas turbine operation has yet to be thoroughly studied.

(3) Among the numerous simulation studies on solar gas turbine system, few of them take a further look into the real-time control behaviors or consider the influence of short-term DNI disturbances. Transient analysis on the components' responses after command execution, for example, the overshoot effects and response rates of the critical parameters, is significant for the control method improvement. Moreover, most of the dynamic analyses have the time step

of 15 min to 1 h which could barely reflect the fluctuant nature of solar irradiance. Severe short-term DNI drop could endanger system operation especially for high-concentration-ratio CSP plants. The system real-time control effect against transitory DNI disturbance needs more research attentions.

In the view of the concluded research gaps, following are the objectives of the present work:

(1) Develop and validate the solar-MGT-TCES thermodynamic model, and based on this, investigate the operation and control strategies aiming for stable operation, including the simultaneous control of N and TOT which utilizes the participation of TCES.

(2) Compare the advantages and disadvantages of the strategies considering power demand, DNI conditions and TCES charging/discharging states, and provide the application recommendation for variant scenarios.

(3) Analyze the transient responses of the critical performance parameters when applying different control strategies to cope with actual DNI disturbances including both transitory and long-term fluctuations. Evaluate the real-time control effects, such as, stabilizing performance and tracing set point.

(4) Discuss the role that TCES plays in system control and compare its compatibility with different operation strategies.

2 System introduction

The solar-MGT-TCES system presented in Fig. 1 is a 10 kW_e recuperated open-loop air Brayton cycle with ambient air serving as heat transfer and working fluid. The design parameters are listed in Table 1. The ambient air is compressed and preheated by a compressor and a recuperator, respectively. The pressurized air is then heated to over 1073 K by a tubular solar air receiver. The following TCES unit can stabilize the TIT against DNI fluctuation and also prolong the generation time by redistributing solar energy in the time dimension. The high-temperature pressurized air then expands in turbine which drives the high-speed alternator (HSA) to generate electricity. The HSA serves as a motor and a generator during the startup/shutdown and self-sustaining process, respectively. The generated alternating current is then regulated to meet grid demand by a rectifier and an inverter. Valve A is a switching valve which would be open in poor DNI condition to avoid thermal losses in receiver. Valve B is a regulating valve to adjust the bypass ratio of TCES and hence the TIT value. When the downstream temperature, such as, TIT and TOT, is too low, the Valve B opening gets bigger to allow more high-temperature air enters turbine directly. The concentrated solar flux can be provided by a parabolic dish or a heliostat field. In this work, the receiver sub-model is built and validated based on the heliostat field parameters in the solar tower test rig in Zhejiang University, China. It should be noted that to focus on the control strategies other than fuel combustion, the studied system is a solar-only MGT system without combustion chamber.

The centrifugal compressor and the radial turbine are designed by City, University of London. The rated rotational speed is designed to be 120 krpm (Table 1) considering the facts that on the one hand, the small weight of MGT rotor results in small torque and hence a high rotational speed; on the other hand, the short blade length requires a higher tip velocity to ensure the compression performance. The counterflow recuperator is designed by Samad Power Ltd. The high-temperature solar air receiver and the cobalt-oxide-based TCES unit are designed by Zhejiang University.

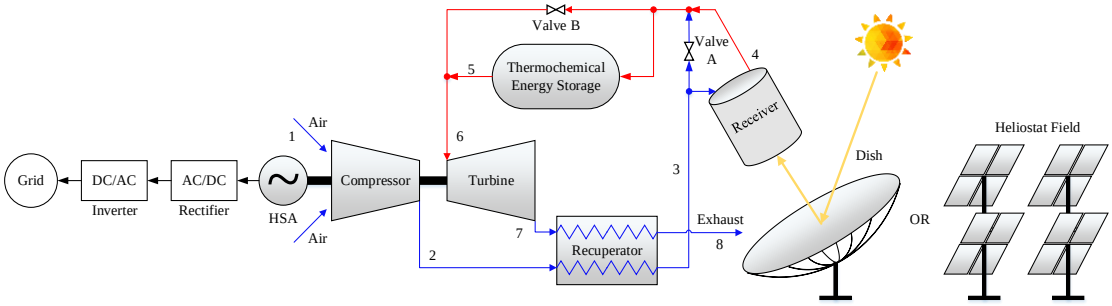

Fig. 1. Scheme of the studied solar-MGT-TCES system

Table 1. Design parameters

Parameters	Values	Parameters	Values
DNI	800 W/m^2	Power output	10 kW$_e$
N	120 krpm	Compressor pressure ratio	3.0
TIT	1073 K	Recuperator effectiveness	0.85
TOT	923 K	Air mass flow rate	0.16 kg/s

3 Methodology

3.1 Thermodynamic model

3.1.1 Assumptions

In this study, a thermodynamic model was developed in MATLAB/Simulink. Appropriate assumptions, not leading far from reality, were made, also reducing computational efforts:

a) The air was treated as a semi-ideal gas, which follows the ideal gas law with other thermophysical properties (e.g., specific heat, viscosity, etc.) variable with temperature. The calculation was derived from the NIST REFPROP.

b) The thermodynamic changes in the pipes and connections (e.g., pressure loss, heat loss, etc.) were omitted.

c) There was no flow leakage, assuming appropriate sealing.

d) Natural convection heat losses in the compressor, turbine, and recuperator were not considered.

The modeling equations are introduced below, followed by each component's validation results summarized in Table 2.

3.1.2 Turbomachinery

The transient response of the turbomachinery components is much faster than that of the heat exchangers. To reduce the computation time while preserving the necessary precision, the compressor and turbine were modeled with zero-dimension quasi-steady-state equations by linear interpolation in the performance maps (e.g., Fig. 14). Based on the isentropic relationship, the outlet temperatures were calculated by Eqn. (1) and (2), respectively (Cohen et al., 1996). The model was validated against the test data from the German Aerospace Center (DLR) with A Turbel T100PH Series 3 (Hohloch et al., 2010) (see Table 2). Noted that the validation model uses the turbel T100PH Series 3 performance map from the literature (Hohloch et al., 2010), while the simulation model in this work uses the characteristic curves of the 10 kW$_e$ MGT designed by City, University of London.

$$T_{02} = T_{01}\left(1 + \frac{PR^{\frac{\gamma-1}{\gamma}} - 1}{\eta_c}\right) \tag{1}$$

$$T_{07} = T_{06}\left[1 - \eta_t\left(1 - \frac{1}{ER^{\frac{\gamma-1}{\gamma}}}\right)\right] \tag{2}$$

where T_{01}, T_{02}, T_{06} and T_{07} are the temperature of compressor inlet and outlet, and turbine inlet and outlet, respectively, PR and ER are pressure ratio and expansion ratio, respectively, η_c and η_t are the isentropic efficiencies of compressor and turbine, respectively, γ is the ratio of air specific heat at a constant pressure and a constant volume.

3.1.3 Heat exchangers

The heat exchangers' internal airflow channels are complicatedly designed, resulting in advanced convective performance and complex 3-D property distributions. Such refined information causes limited contributions to the control strategy investigation while consuming massive computational efforts, so the "lumped-volume" approach (Traverso, 2004) was adopted in the recuperator and receiver model. TCES adopted the 1-D finite element method, considering its large thermal inertia. The time-dependent behaviors were acquired by mass and energy conservation.

3.1.3.1 Recuperator

The recuperator core was simplified into a metallic mass of uniform thermophysical properties with hot and cold air passing by each side reversely. The outlet temperature was calculated by Eqn. (3) through (5), among which, the heat transfer coefficients were constant values provided by the manufacturer, and the lumped mass was the core weight. The pressure drop is a function of the mass flow rate. Model validation was also conducted against the test results by DLR (Hohloch et al., 2010) (see Table 2).

$$MC_{p,M}\frac{dT_M}{dt} = \dot{Q}_h - \dot{Q}_c \tag{3}$$

$$\dot{Q}_h = \dot{m}_h C_{p,h}\left(T_{h,in} - T_{h,out}\right) = U_h A_h\left(\frac{T_{h,in} + T_{h,out}}{2} - T_M\right) \tag{4}$$

$$\dot{Q}_c = \dot{m}_c C_{p,c}\left(T_{c,out} - T_{c,in}\right) = U_c A_c\left(T_M - \frac{T_{c,in} + T_{c,out}}{2}\right) \tag{5}$$

Where M is the mass of recuperator core, $C_{p,M}$, $C_{p,h}$ and $C_{p,c}$ are the specific heat of recuperator core, hot-side air and cold-side air, respectively, T_M, $T_{h,in}$, $T_{h,out}$, $T_{c,in}$ and $T_{c,out}$ are the core temperature and the temperature of hot-side inlet, hot-side outlet, cold-side inlet and cold-side outlet, respectively, $\dot{Q}_h$ and $\dot{Q}_c$ are the energy fluxes of hot-side and cold-side, $\dot{m}_h$ and $\dot{m}_c$ are

the mass flow rate of hot-side and cold-side, U_h and U_c are the overall heat transfer coefficients of hot-side and cold-side, A_h and A_c are the overall heat transfer areas of hot-side and cold-side.

3.1.3.2 Receiver

The air receiver was a double-stage-heating tube-cavity receiver, as shown in Fig. 2. Two staggered circles of tubes, called inlet and outlet circles, were connected by a ring. Air entered the inlet circle heated by solar irradiance and flowed back through the outlet circle, continuing to absorb energy. The lumped mass was the sum of the tubes and their connection ring. The internal heat transfer calculation used convection correlations for turbulent pipes (Gnielinski, 1976). The outlet temperature was derived from Eqn. (6) to (9) (Azzouzi et al., 2017). Pressure losses considered both frictional loss in the tubes and local loss in the bends and rings. Heat losses included the radiative and convective losses through the aperture as well as the conductive and convective losses through the radial and bottom surfaces. Under design condition, the receiver inlet and outlet temperature are 808 K and > 1073 K, respectively. The validation experiments were conducted in the solar tower test rig at Zhejiang University in China (see Table 2). For detailed information of the test, please see Appendix A.

$$MC_{p,M}\frac{dT_M}{dt} = \dot{Q}_{in} - \dot{Q}_{loss} - \dot{Q}_{use} \tag{6}$$

$$\dot{Q}_{in} = DNI \cdot A_{mir} \cdot \eta_{field} = \varepsilon\sigma A_{icav}\left(T_{wicav}^4 - T_{amb}^4\right) \tag{7}$$

$$\dot{Q}_{loss} = \left(U_{ar}A_{ar} + U_{ac}A_{ac} + U_r A_r + U_z A_z\right)\left(T_{wicav} - T_{amb}\right) \tag{8}$$

$$\dot{Q}_{use} = \dot{m}C_{p,m}\left(T_{out} - T_{in}\right) = h_{conv}A_{conv}\left(T_M - \frac{T_{in} + T_{out}}{2}\right) \tag{9}$$

where M is the lumped mass, $C_{p,M}$ and $C_{p,m}$ are the average specific heat of lumped mass and airflow, respectively, T_M, T_{wicav}, T_{amb}, T_{in} and T_{out} are the temperature of lumped mass, inner cavity wall, ambient air, inlet and outlet airflow, $\dot{Q}_{in}$, $\dot{Q}_{loss}$ and $\dot{Q}_{use}$ are the concentrated solar flux, thermal losses and the absorbed heat by airflow, U and A are the overall heat transfer coefficient and area, respectively, the abbreviations ar, ac, r, z, $conv$ and $icav$ refer to radiative heat loss through aperture, convective heat loss through aperture, radial heat loss, bottom heat loss, convective heat transfer and the internal cavity, $\dot{m}$ is the mass flow rate of airflow, h_{conv} is the convective heat transfer coefficient.

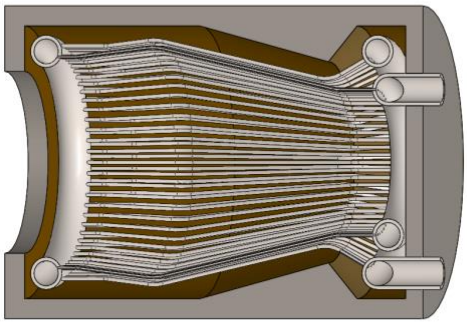

Fig. 2. The internal structure of the receiver

3.1.3.3 TCES

TCES utilizes the reversible redox reaction of cobalt and cobaltous oxide (Co_3O_4/CoO pair) (Eqn. (10)) to obtain high energy storage density. In the present reactor, cobalt oxide and cordierite powders were pressed into honeycomb cubes piled into layers and sealed by stainless steel casing and insulation. The modeling approach was derived from the work outlined in (Zhou et al., 2019) and (Singh et al., 2017) and improved upon by adding the thermal loss term in Eqn. (11). The reactor core was assumed to be a tube with the length of the stack. The fluid and solid cross-section areas were equal to the total cross-section areas of the channels and solid body, respectively. The thermochemical feature was considered as an additional source term in Eqn. (11) and it was derived from the chemical reaction kinetics in Eqn. (13). The oxygen variations were negligible compared to the inlet airflow. Pressure loss was calculated with the Fanning friction factor (Zhou et al., 2019). The model was validated against the test and simulation results by DLR (Singh et al., 2017) (see Table 2). The validation curves are shown and discussed in Appendix B.

$$Co_3O_4 \leftrightarrow 3CoO + 0.5O_2, \Delta H_r = 196.2\,kJ/mol \tag{10}$$

Solid field:

$$MC_{p,M}\frac{dT_M}{dt} = h_{conv}A_{conv}\left(T_m - T_M\right) + \dot{S}_h - \dot{Q}_{loss} \tag{11}$$

Fluid field:

$$\rho A_{air} L C_v \frac{dT_m}{dt} = \dot{m}_{in}C_{p,in}T_{in} - \dot{m}_{out}C_{p,out}T_{out} - h_{conv}A_{conv}\left(T_m - T_M\right) \tag{12}$$

$$\dot{S}_h = \Delta H_r \cdot R_t \cdot C_t \tag{13}$$

where ΔH_r is the reaction enthalpy, M is the mass of storage core, $C_{p,M}$, $C_{p,in}$ and $C_{p,out}$ are the constant pressure specific heat of storage core, inlet air and outlet air, respectively, C_v is the constant volume specific heat of air, T_M, T_{in}, T_{out} and T_m are the core temperature, inlet and outlet air temperature and the average of inlet and outlet air temperature, respectively, h_{conv} is the convective heat transfer coefficient, A_{conv} and A_{air} are the convenctive heat transfer area and cross section area of fluid field, respectively, $\dot{S}_h$ and $\dot{Q}_{loss}$ are the energy fluxes of chemical reaction and heat loss,

respectively, ρ is the density of airflow, L is the length of the stack, $\dot{m}_{in}$ and $\dot{m}_{out}$ are the inlet and outlet mass flow rate, respectively, R_t is the reaction rate, C_t is the reaction concentration.

3.1.4 Power electronics

The power electronics module included an HSA, a rectifier, and an inverter. It updated the N according to the angular momentum variation of the shaft (Eqn. (14) ~ (15)) (Ghavami et al., 2017).

$$J\frac{d\omega}{dt}=\frac{1}{\omega}PW_{net} \tag{14}$$

$$PW_{net}=PW_{gt}-PW_{load}/\eta_{HSA}\eta_{REC}\eta_{INV} \tag{15}$$

where J is the rotational mechanical inertia, ω is the angular rotational speed, PW_{net}, PW_{gt} and PW_{load} are the system net power output, gas turbine power output and load power, respectively, η_{HSA}, η_{REC} and η_{INV} are the efficiency of HAS, rectifier and inverter, respectively.

3.1.5 System integration

For system integration, the mass continuity and inter-connecting plena approach were compared (Traverso, 2004). The mass continuity approach ignores the delays inherent to mass transfer and allows larger time steps, which shortens calculation time but sacrifices precision. The interconnecting plena approach calculates the pressure variations according to the inflow and outflow mass of the components (Eqn. (16)). Because of the volumetric effects in TCES, the interconnecting plena approach was adopted here. The time step of the transient simulations below is 0.1 second.

$$\frac{dP}{dt}=\frac{R_gT}{V}\left(\dot{m}_{in}-\dot{m}_{out}\right) \tag{16}$$

where P, T and V are the pressure, temperature and volume of the component, respectively, R_g is the gas constant, $\dot{m}_{in}$ and $\dot{m}_{out}$ are the inlet and outlet mass flow rate.

Table 2 summarize the validation results of the components models. The listed critical parameters were compared with the test data from literatures and in-house experiment. Each of them included several operating points, so the maximum deviations were shown. For more details and discussions about the receiver and TCES validations, please refer to Appendix A and B.

Table 2. Validation results of the component models

Parameters	Deviation	References
Compressor outlet temperature	< 3.2%	(Hohloch et al., 2010)
Compressor outlet pressure	< 6.0%	
Recuperator cold-side outlet temperature	< 3.9%	
Recuperator hot-side outlet temperature	< 6.0%	

Recuperator cold-side outlet pressure	< 0.3%	
Recuperator hot-side inlet pressure	< 3.3%	
Receiver outlet temperature	< 5.0%	In-house experiment (see Appendix A)
TCES outlet air temperature (charging)	< 4.6%	(Singh et al., 2017)
TCES outlet air temperature (discharging)	< 6.6%	
TCES middle solid temperature (charging)	< 8.2%	
TCES middle solid temperature (discharging)	< 11.2%	
TCES top solid temperature (charging)	< 8.8%	
TCES top solid temperature (discharging)	< 5.3%	

3.1.6 Simplifications of the steady-state analysis

Several simplifications were made for the steady-state analysis. For TCES, the reduction and oxidation reactions would not be triggered until the reactant reaches a specific temperature. Once the reaction begins, with steady boundary conditions, the outlet temperature would stay at a "platform value," i.e., T_{chr} ≈1120 K and T_{disc} ≈1155 K for reduction and oxidation, respectively, until the conversion rate reaches its limit (Spelling et al., 2014) (see Fig. 18 in Appendix B). Thus, the steady-state analysis was based on platform temperatures.

Moreover, results that satisfy any of the following conditions were excluded: (1) No positive net power output; (2) receiver outlet temperature, $T_{rcv,out}$, TIT or TOT exceeding the material constraints of heat-absorbing tubes, turbine and recuperator, i.e., 1255 K, 1073 K ± 5 K and 923 K ± 5 K, respectively. Although a certain accuracy is sacrificed, the reflected pattern is of an important reference value.

3.2 Operation and control strategies

Four typical operation strategies are proposed for the solar-MGT-TCES system for different applications, i.e., constant N, constant TIT, constant TOT, and maximum overall efficiency strategies. Constant N is meaningful for stable electric voltage supply, which is linearly related to the HSA frequency. Constant TIT/TOT at the design point allows the MGT to approach its optimal efficiency.

For a high-percentage-solar-share MGT system, there are two main challenges to system control: the inapplicability of fuel combustion and the large thermal inertia of the heat exchangers. Conventional gas turbines use fuel flow adjustment to cope with load change because of its rapid response. However, in this case, it is impractical to adjust the fuel (solar irradiance) to cope with sudden load change. Furthermore, due to the large thermal inertia, the time constants of the heat exchangers (minute-order) are orders of magnitude larger than those of turbomachinery and power electronics components (millisecond-order). Because the discordance between the compressor and turbine might lead to dangerous situations such as surging or choking, it is critical to improve the response speed of the heat exchangers.

By adjusting the output power fed into the grid, the N in HSA and MGT can be controlled along with the other parameters, e.g., TIT, TOT, etc., because of the system's highly coupled nature (Ghavami et al., 2017). The flexibility of TCES (TES) participation can also be utilized in system control (Rovense et al., 2019). Thus, the output power and the TCES bypass ratio were selected as the new manipulated variables to accomplish different operation strategies. The transient simulations analyzed the control effect with real-world DNI variation.

3.2.1 Constant N control with power regulation

For constant N operation, a single PI (proportion integration) controller is sufficient. The block diagram in Fig. 3 demonstrates where the rotational speed set point N_{set} and the base value of output power $PW_{load,0}$ are the design points (120 krpm and 10 kW_e, respectively) and the N deviation ΔN and power adjustment PW_{load} are the input and output of the PI controller, respectively. The PI controller parameters, proportion constant K_p and integration constant K_i, are both 8.

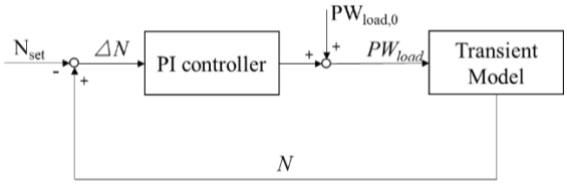

Fig. 3. Schematic diagram of constant N control

3.2.2 Constant TOT control with power regulation

For constant TOT operation, cascade control of the two PI controllers is required to overcome the time constant gap. As shown in Fig. 4, the first PI controller regulates the N_{set} according to TOT deviation ΔTOT, while the second ensures that the N follows the N_{set} closely by power regulation. The first PI controller serves as a buffer by reducing the N response. Otherwise, the turbine might overspeed before TOT reaches its set point TOT_{set}, i.e., the design value of 923 K. The PI controller in the inner loop is the same as that in constant N control. The parameters of the PI controller in the outer loop, K_p and K_i, are 30 and 300, respectively.

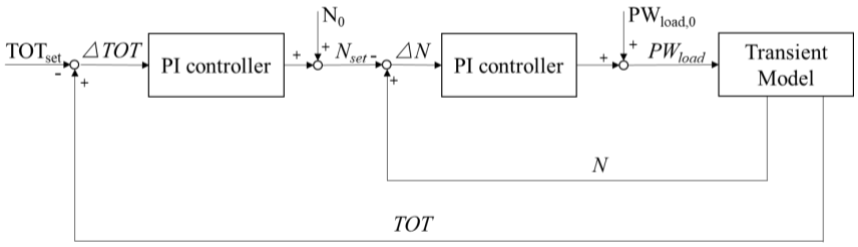

Fig. 4. Schematic diagram of constant TOT control

3.2.3 Constant N-TOT simultaneous control with power and bypass regulation

Despite the highly coupled nature of the solar-MGT-TCES system, simultaneous control of N and TOT can be accomplished by combining power and bypass regulations. Here, the bypass regulation is implemented by the regulating the valve B in Fig. 1. As shown on the left of Fig. 5, there are two control loops: one adjusts the power according to the N deviation by a PI controller, while the other outputs the

valve opening (VO) instruction according to the TOT deviation using an anti-windup PID (proportion integration differentiation) controller. The PI controller for power regulation is the same as that in constant N control. The anti-windup PID controller is based on an industrial PID controller, the parameters of which are: proportion gain K_c = -0.0003, integration time T_i = 1, differentiation time T_d = -3, differentiation gain A_d = 3.

With N and TOT constant, the operation point of a gas turbine is essentially fixed (see 4.2.4.1, where the design point is used as an example [120 krpm and 923 K TOT]). This requires adequate energy to support high-performance operation, so a DNI threshold value (DNI_{tsh}) is proposed for mode switching, as illustrated in Fig. 5. When the weather conditions or energy storage cannot meet the power demand for N-TOT simultaneous control, constant N operation with power regulation is implemented. At this point, the uncontrolled TCES bypass VO remains constant. Thus, the choice of DNI_{tsh} and the original VO (VO_0) is also discussed below in order to improve system performance.

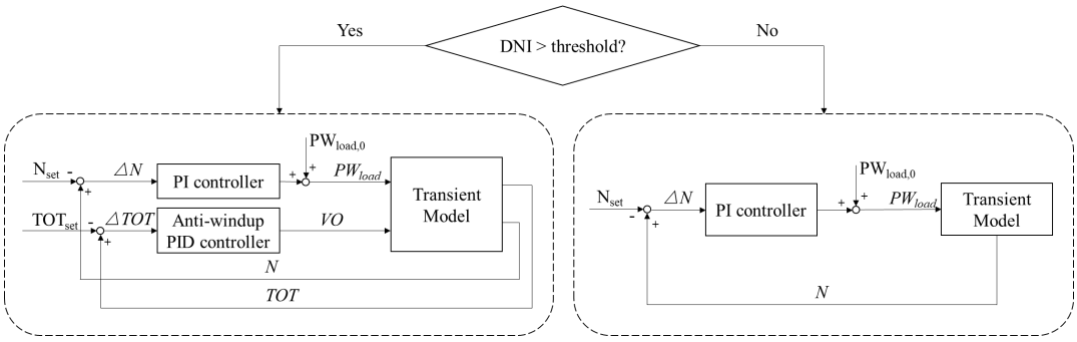

Fig. 5. Schematic diagram of constant N and TOT simultaneous control

4 Results and discussion

4.1 Steady-state analysis of operation and control strategies

4.1.1 Charging state

Fig. 6 compares the operation strategies under various DNI and VOs conditions. For constant TOT operation (Fig. 6 (a)), TCES only takes effect when DNI was > 720 W/m^2, where curves of different VOs do not overlap with each other. As VO decreased, more energy was stored rather than producing electrical output, yet implying a broader adjustable range between 10 and 15 kW$_e$. Constant N operation (Fig. 6 (b)) without TCES (VO = 100%, full bypass) required the smallest range of least DNI values (450 ~ 850 W/m^2). Low DNI conditions cannot meet the power demand for design point rotation, while high DNI condition causes surplus energy, requiring energy storage. Otherwise, the turbine and recuperator would overheat. As VO decreased, more air flowed into TCES, and the applicable DNI range of constant N operation increased. When all the air entered TCES, the output power remained at 11 ~ 13 kW$_e$.

In contrast, for constant TIT and maximum efficiency operations (Fig. 6 (c) and (d)), the clusters of all VOs were essentially covering each other, indicating that the TCES participation imposed little impact on output performance. This is partially caused by the simplifications taken in the steady-state model.

The TIT (1073 K) was set below T_{chr} (1120 K), so with limited temperature drop in TCES, TIT would be excessive, no matter how much air was bypassed through the system.

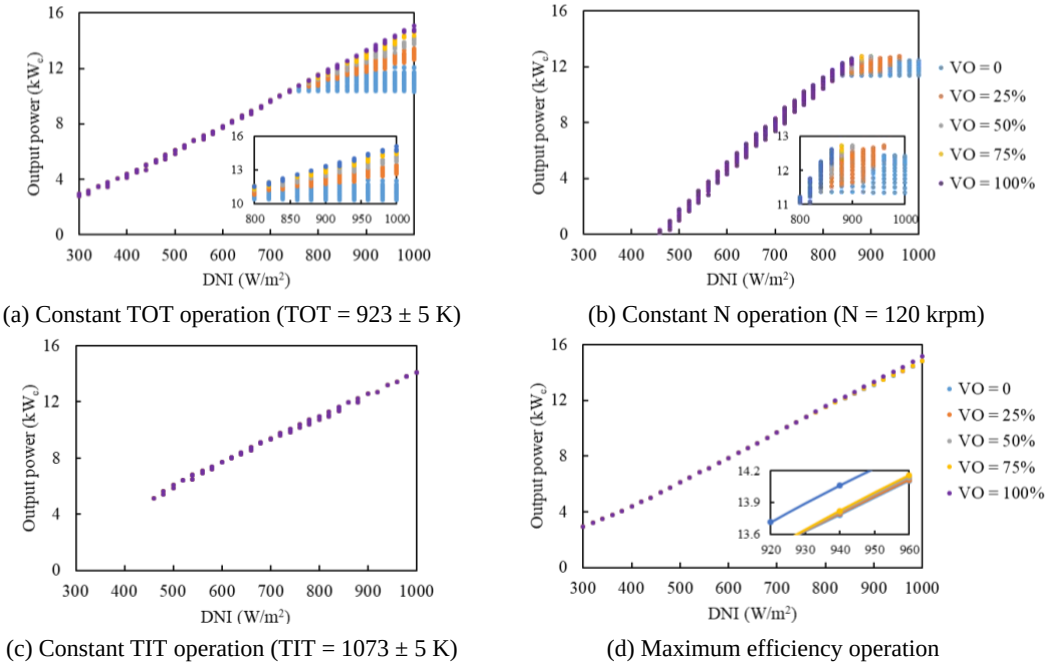

(a) Constant TOT operation (TOT = 923 ± 5 K)

(b) Constant N operation (N = 120 krpm)

(c) Constant TIT operation (TIT = 1073 ± 5 K)

(d) Maximum efficiency operation

Fig. 6. Comparison of operation strategies under various DNI and VOs (charging state)

Moreover, it can be seen in Fig. 7 that constant TOT and constant TIT were very close to the maximum efficiency performance, indicating the replaceability of the latter. The output power was more sensitive to DNI in constant N operation (12 kW_e change per 350 W/m^2). Under no-bypass circumstances (Fig. 7 (a)), constant TOT compromised the efficiency but still could output more than 10 kW_e. This helps to exploit the potential of TCES while guaranteeing satisfactory system performance.

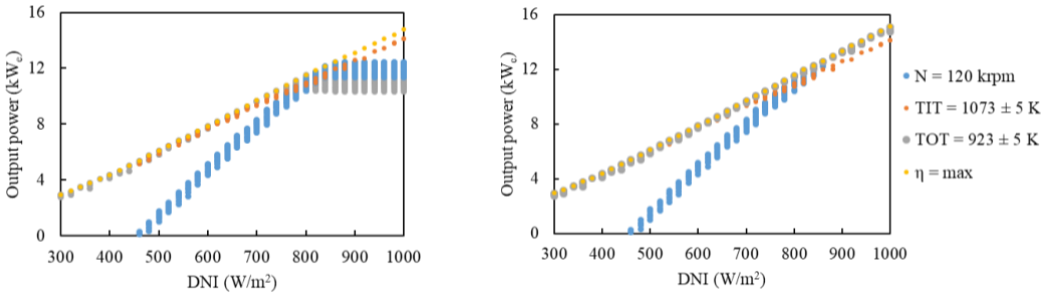

(a) No-bypass condition

(b) Full-bypass condition

Fig. 7. Comparison of no- and full-bypass conditions under various DNI and operation strategies (charging state)

In summary, for the charging state, constant TOT operation has the highest flexibility and applicable DNI range. It can cope with all DNI conditions by power regulation and TCES bypass regulation. Constant N operation is the second-best flexible choice for power and bypass regulation, but it sacrifices efficiency and is only applicable for a specific DNI range. Although maximum efficiency and constant TIT operations ensure the best system efficiency, they only work with power regulation.

4.1.2 Discharging state

During discharging, the solar radiation and the energy stored in TCES work as the "fuel," so the VO imposes more apparent effects on system performance, as shown in Fig. 8 and Fig. 9. In general, as VO increases, the slope of the cluster increases, indicating a narrower applicable DNI range as well as a broader controllable output power range. The slopes of large VO lines with constant N operation (Fig. 8 (b)) and those of the small VO lines with constant TIT operation (Fig. 8 (c)) are the steepest (~3 kW_e change per 100 W/m^2), indicating that the output power needs quicker rates of change to handle the DNI fluctuations under these circumstances.

The area enclosed by all the clusters implies the overall operational zone. Constant TOT operation covers the broadest operational zone (Fig. 8 (a)), indicating that it has the highest flexibility with power and bypass regulation. For constant N and constant TIT operations (Fig. 8 (b) and (c)), there are only four clusters. This is because when VO = 0, the TCES outlet temperature exceeds the TIT limit and causes the turbine to overspeed.

In constant TOT and maximum efficiency operations (Fig. 8 (a) and (d)), when VO < 50%, the output power is more stable (< 1.3 kW_e and < 0.75 kW_e per 100 W/m^2, respectively). Overall, steady power generation is achievable with bypass regulation. When VO > 50%, the output power responds more sensitively with DNI fluctuations, so power regulation adjusts based upon changes in DNI. Moreover, constant TOT and maximum efficiency operations are feasible under a full DNI span without overheating or overspeed, and generate more electricity than constant N and constant TIT operations (Fig. 8 (b) and (c)).

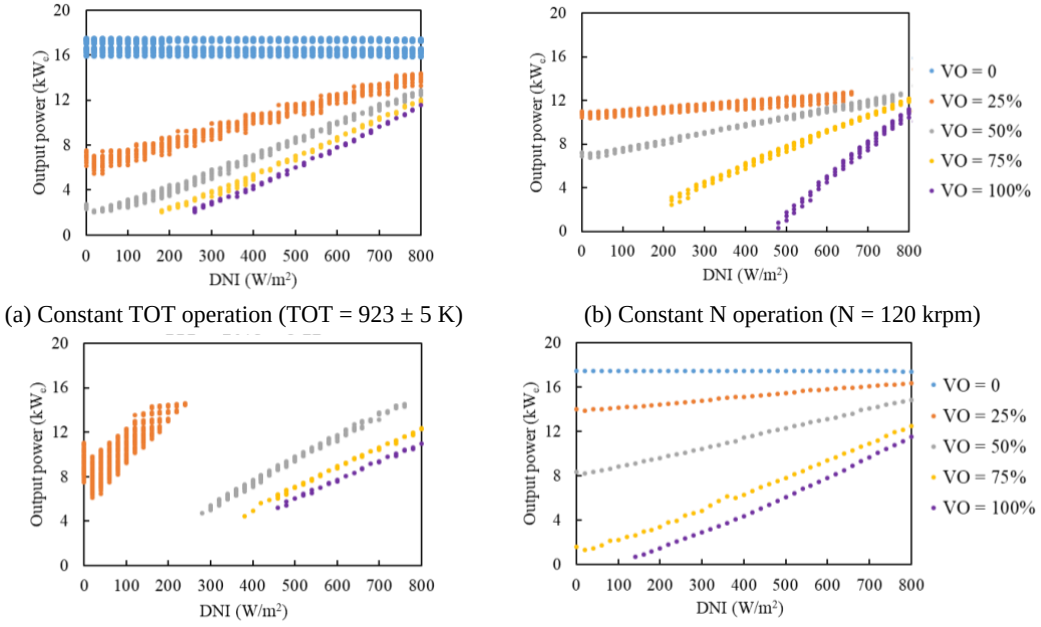

(a) Constant TOT operation (TOT = 923 ± 5 K)

(b) Constant N operation (N = 120 krpm)

(c) Constant TIT operation (TIT = 1073 ± 5K)

(d) Maximum efficiency operation

Fig. 8. Comparison of operation strategies under various DNI and VOs (discharging state)

Because a "no-bypass" condition is not available in constant N and constant TIT scenarios, 1/4-bypass, and full-bypass conditions are compared instead, as shown in Fig. 9. The pattern of the full-bypass condition (Fig. 9 (b)) is similar to that of the charging state results (Fig. 7 (b)). However, as demonstrated in Fig. 9 (a), the TCES participation elevated the output power level in all operation

strategies, compared to Fig. 9 (b). The applicable DNI ranges increase as well, except under the condition of constant TIT operation. Because TIT is directly affected by TCES and the TIT design point (1073 K) is close to T_{disc} (≈ 1155 K), this small temperature gap limits the flexibility of $T_{rcv,out}$, which is reflected in the applicable DNI range.

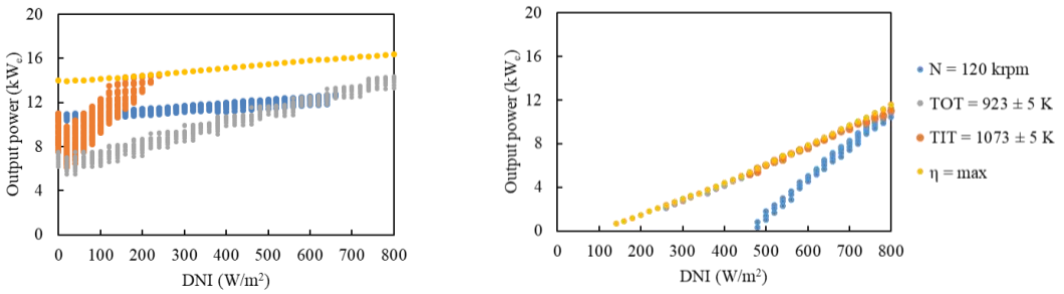

(a) 1/4-bypass condition (b) Full-bypass condition

Fig. 9. Comparison of 1/4- and full-bypass conditions under various DNI and operation strategies (discharging state)

As summarized in Table 3, the choices for operation and control strategies depend on the power demand and climate conditions. Constant N operation is suitable for steady electric voltage supply, and its performance varies most from the other strategies, but DNI restricts its application scenario. To meet the higher power demand, constant TOT operation is the first recommendation because of its largest operational zone and highest flexibility.

Table 3. Summary of the application scenarios of operation and control strategies

		Application scenarios	
		Power regulation	Bypass regulation
Charge	Constant N (120 krpm)	0 ~ 12 kW_e, 450 ~ 850 W/m^2	0 ~ 100 %, > 850 W/m^2
	Constant TOT (923 K)	0 ~ 15 kW_e, full DNI scope	0 ~ 100 %, > 750 W/m^2
	Constant TIT (1073 K)	5 ~ 14 kW_e, > 450 W/m^2	-
	Maximum efficiency	0 ~ 15 kW_e, full DNI scope	-
Discharge	Constant N (120 krpm)	0 ~ 12 kW_e, full DNI scope	0 ~ 100 %, full DNI scope
	Constant TOT (923 K)	2 ~ 18 kW_e, full DNI scope	0 ~ 100 %, full DNI scope
	Constant TIT (1073 K)	5 ~ 14 kW_e, full DNI scope	0 ~ 100 %, full DNI scope
	Maximum efficiency	1 ~ 18 kW_e, full DNI scope	0 ~ 100 %, full DNI scope

4.2 Transient analysis on operation and control strategies

4.2.1 Constant N control with power regulation

Fig. 10 shows the system response under actual DNI conditions measured by the solar tower test rig in Zhejiang University, China, on May 18th, 2017. For convenience, the time axis refers to the simulation time instead of actual time. Simulations started at 400 W/m^2 (6:40 AM) when the net output power was positive. The DNI variation (Fig. 10 (a)) included a transitory harsh drop at 5.5 h and an extensive low period at 8 h, representing critical input conditions. The performance of no-, half- and full-bypass situations were compared to study the influence of TCES participation. To be clear, in Fig. 10 (b), the chemical energy flux is calculated by Eqn. (13), and the sensible energy flux is the difference between the total energy flux in TCES core and the chemical energy flux. The same goes for the discussion in the following sections.

The maximum deviations of N and mass flow rate were 0.003% (3 rpm) and 5.8% (0.01 kg/s), respectively. The design point (10 kW_e) was achieved at above 700 W/m^2. The large thermal inertia of the TCES safeguarded against the DNI variation and smoothed the performance curves with 15% ~ 20% less fluctuation. With TCES, the climbing rates of the output power, receiver temperature and turbine temperature (Fig. 10 (a), (c), and (d)) were reduced, and the performance drops caused by a DNI reduction were delayed and overall lessened. The transitory DNI drop at 5.5 h barely affected the system performance, while the long DNI drop at 8 h caused evident declines in power output. Thus, when confronting sudden extreme weather, MGT parameters can be better stabilized by enhancing the participation of TCES.

The TCES participation prolonged the generation time by 1 h. The endothermic reduction reaction was not triggered until 4 h when $T_{rcv,out}$, reached 1050 K (Fig. 10 (b) and (c)). The exothermic oxidation reaction started immediately when DNI was reduced to 700 W/m^2 at 7 h, and lasted for nearly 2 h, while the sensible heat continued to be released. The released sensible energy flux became stronger throughout the last two hours because of the lower inlet temperature and a higher mass flow rate in TCES. The difference between half- and no-bypass curves is inconspicuous, indicating that the participation degree of TCES had limited influence on system performance, and more energy can be stored without significantly sacrificing short-term power generation.

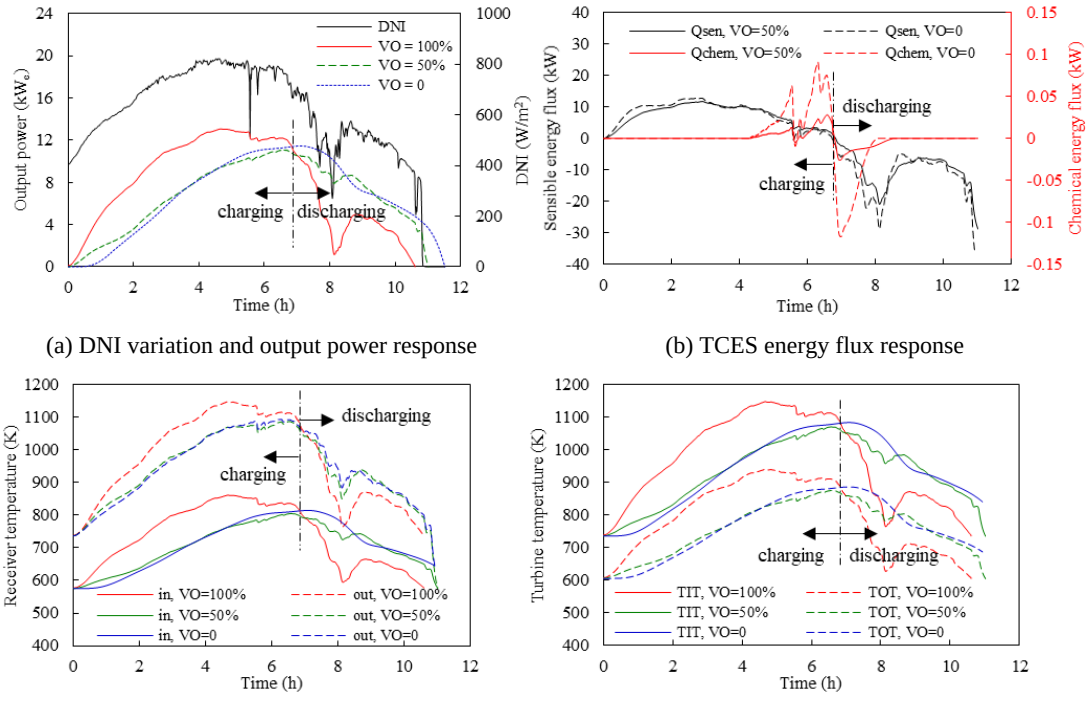

(a) DNI variation and output power response

(b) TCES energy flux response

(c) Receiver temperature response

(d) Turbine temperature response

Fig. 10. System response of constant N control with power regulation

4.2.2 Constant TOT control with power regulation

As shown in Fig. 11, the simulation started at 150 W/m^2 (5:45 AM), less than that of constant N, because generation can begin well before 150 W/m^2 by slowing down N. The maximum TOT deviation was 0.07% (< 1 K). Although the mass flow rate ranges in both cases widely differed (0.16 ~ 0.17 kg/s in constant N and 0.06 ~ 0.16 kg/s in constant TOT), the output power variations were similar (0 ~ 12.7

kW_e, Fig. 10 (a) and Fig. 11 (a)). When DNI was over 700 W/m^2, the system performance was maintained in an optimal state.

The no-bypass responses display a smooth-but-drastic pattern. Because $T_{rcv,out}$ (dashed lines in Fig. 11 (c)) was high enough to trigger the reduction reaction initially (Fig. 11 (d)), the thermal inertia and the time delay were intensified. The TCES participation also prolonged operation by 1 h (Fig. 11 (a)). The charging and discharging appear alternately due to $T_{rcv,out}$ varying near the reaction temperature. The potential of TCES is better exploited in this scenario as more heat can be stored thermochemically, yet low VO operation is not recommended due to operational safety issues.

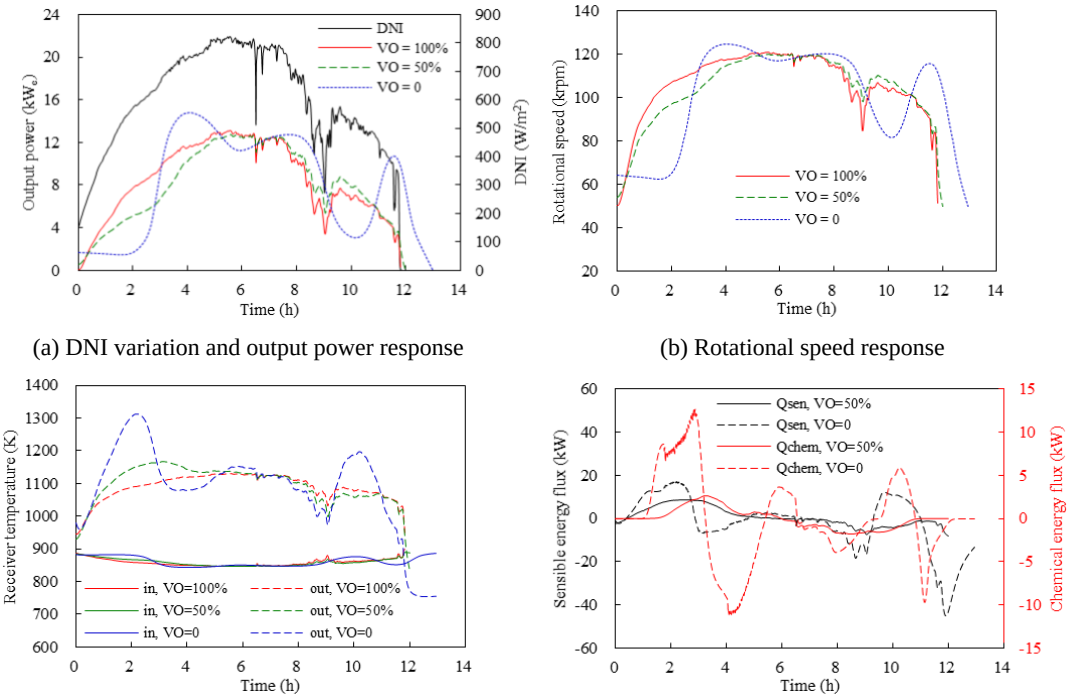

(a) DNI variation and output power response

(b) Rotational speed response

(c) Receiver temperature response

(d) TCES energy flux response

Fig. 11. System response of constant TOT control with power regulation

4.2.3 Constant N-TOT simultaneous control with power and bypass regulation

4.2.3.1 Influence of DNI_{tsh}

To determine an optimal DNI_{tsh}, VO_0 was set to 50%. The output power was kept constant at 12.6 kW_e ± 4% with DNI varying between 750 and 820 W/m^2, plus a transitory steep decrease to 500 W/m^2 at 6 h (Fig. 12 (a)). The maximum deviation of N was 0.003% (3 rpm), while the maximum TOT deviation during simultaneous control periods largely depended on the DNI_{tsh} (17 K, 4 K, and <1 K for DNI_{tsh} = 750 W/m^2, 700 W/m^2, and 650 W/m^2, respectively).

The switching duration and degree of overshoot are affected by DNI_{tsh} as well. It took 1.1 h, 0.7 h and 0.5 h to stabilize both N and TOT (Fig. 12 (b)) for 650 W/m^2, 700 W/m^2 and 750 W/m^2 DNI_{tsh},

respectively. With DNI_{tsh} values of 650 W/m^2 and 700 W/m^2, TIT and TOT overshot by 5.1% and 5.3%, respectively, while only a 2% overshoot when DNI_{tsh} was 750 W/m^2 (Fig. 12 (b)). These characteristics were reversed at the transitory DNI drops during simultaneous control. Overall, more heat was thermochemically stored in TCES when DNI_{tsh} = 750 W/m^2 (Fig. 12 (d)).

For application, a higher DNI_{tsh} value is recommended for clear sunny days, while lower DNI_{tsh} values are more advantageous on cloudy days.

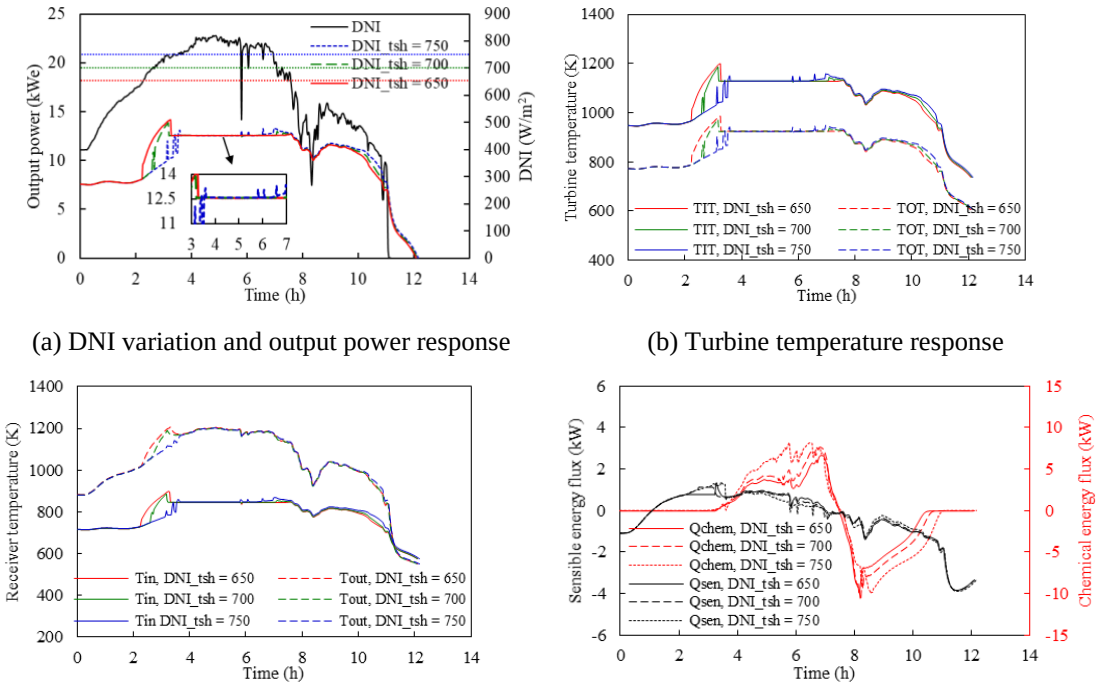

(a) DNI variation and output power response

(b) Turbine temperature response

(c) Receiver temperature response

(d) TCES energy flux response

Fig. 12. System response of constant N and TOT simultaneous control (influence of DNI_{tsh})

4.2.3.2 Influence of VO_0

Throughout this VO_0 discussion, DNI_{tsh} was set to 700 W/m^2. The output was stabilized at 12.6 kW$_e$ ± 5% (Fig. 13 (a)). The maximum deviation of N was 0.02% (24 rpm), and the maximum TOT deviation during simultaneous control depended on the VO_0 (15 K, <1 K, and 19 K for VO_0 = 75%, 50%, and 25%, respectively). The switching durations lasted for 0.4 h ~ 0.6 h. Thereinto, the 75% VO_0 was the earliest point to start simultaneous control. The degree of over adjusting was half of that of the other two cases, which better avoids overheating in the turbine, recuperator, and receiver (Fig. 13 (b) ~

(c)). During simultaneous control, the variations were < 1%. More energy was stored and released in the 25% VO_0 scenario (Fig. 13 (d)) because of the larger mass flow rate in TCES.

In general, the overshoot effect outweighs the instant fluctuation considering that operation safety should be the priority. Therefore, a large VO_0 should be employed in good weather conditions, while in poor DNI conditions, when the overshoot degree is within the limit, the VO_0 can adequately obtain greater operational stability.

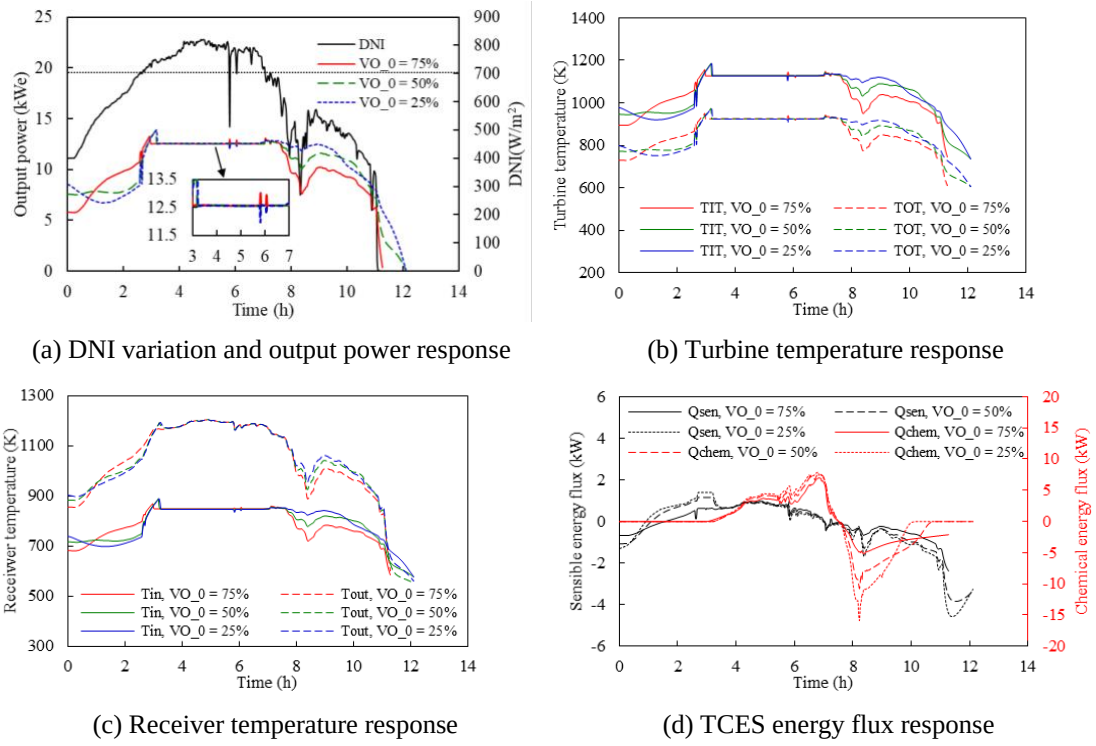

(a) DNI variation and output power response

(b) Turbine temperature response

(c) Receiver temperature response

(d) TCES energy flux response

Fig. 13. System response of constant N and TOT simultaneous control (influence of VO_0)

4.2.4 Comparative analysis of three control strategies

4.2.4.1 Surge and choke risks

Prevention from compressor surging or choking is significant in gas turbine control. Due to the lack of surge and choke line information of the studied MGT, the operation paths derived from the simulations above were exhibited in the compressor performance map to conduct a qualitative analysis, as shown in Fig. 14 (a). Taking the design point and maximum efficiency curve as a reference, the constant N path was almost on the constant corrected speed line of the design point, and the deviations of the corrected mass flow rate and pressure ratio were < 5% and < 3%, respectively. Noted that the corrected speed and corrected mass flow rate in both maps are calculated by Eqn. (17) and (18). This is why the constant N line is not completed of the shape of other constant corrected speed lines. The constant TOT path almost overlapped the maximum efficiency curve with the pressure ratio and N deviated < 4.5% and < 10%, respectively. For N-TOT simultaneous control, the whole path was fixed within 0.4% of the corrected mass flow rate away from the design point.

The turbine performance map is also presented in Fig. 14 (b) to help understanding the operation paths for turbine, which shows some different characteristics. The N-TOT simultaneous control line no longer adheres to the design point and instead, it overlaps with the constant N line. For both cases, as the corrected speed gets higher (N gets higher or TIT gets lower relatively), the turbine isentropic efficiency becomes lower. The constant TOT line also stays close to maximum efficiency. However, there appears a certain amount of operation points in low ER and low corrected speed area which is caused by the drop of rotational speed when DNI is insufficient.

In general, the operation paths are far away from the surging area (left end of the constant corrected speed lines in compressor map) and the choking area (the vertical lines in compressor map and the horizonal lines in turbine map), so the simulated cases were at low risk of surging or choking (Dixon, 2005).

$$\dot{m}_{corrected} = \frac{\dot{m}\sqrt{T_{in}}}{P_{in}}\left(kg \cdot K^{0.5} \cdot s^{-1} \cdot bar^{-1}\right) \tag{17}$$

$$N_{corrected} = \frac{N \cdot \pi}{30\sqrt{T_{in}}}\left(rad \cdot K^{-0.5}\right) \tag{18}$$

where $\dot{m}_{corrected}$ and $N_{corrected}$ are the corrected mass flow rate and corrected rotational speed, respectively, $\dot{m}$ is the mass flow rate, T_{in} and P_{in} are the inlet temperature and pressure, respectively, N is the rotational speed, rpm, π is the circular constant.

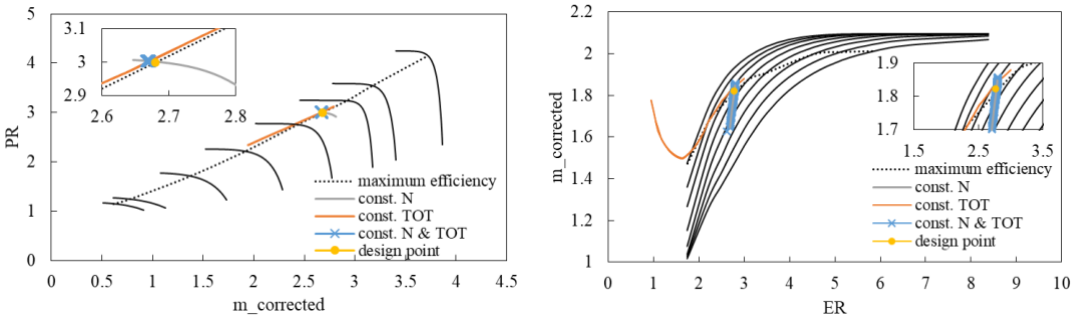

(a) Compressor (b) Turbine

Fig. 14. Operation paths of three control strategies on the performance maps

4.2.4.2 TES performance

The chemical and sensible thermal energy variations in TCES are compared in Fig. 15, including no- and half-bypass cases when applying constant N and constant TOT strategies, as discussed in section 4.2.1 and 4.2.2. The presented charged and discharged energies are the integral of the corresponding energy flux curves in the former sections.

By keeping N constant, the mass flow rate was held at a high level, causing a low $T_{rcv,out}$ and causing difficulties for TCES to absorb heat (≈ 50 kWh) in both chemical (< 0.1 kWh) and sensible (≈ 50 kWh) forms. The same pattern is observed for discharging due to the limited energy storage.

The influence of VO was more evident with a constant TOT due to the higher $T_{rcv,out}$. Despite the lower mass flow rate in the half-bypass case, a higher temperature had a more significant influence and resulted in higher energy density of the airflow. When the input airflow mass was halved, a larger amount of energy was lost, giving rise to a larger gap between the energy sums of no-bypass (69.7 kWh) and half-bypass (30.2 kWh). In the no-bypass-constant TOT scenario, there was a sudden drop in $T_{rcv,out}$ from 960 K to 780 K at the end of the simulation (see Fig. 11 (c)), leading to a massive total heat release in TCES (96.5 kWh), which was greater than the amount of stored heat.

In general, constant TOT operation can store up to 32% (16.9 kWh) more energy than constant N when VO = 0 and better exploit the potential of thermochemical characteristics. For a constant TOT operation, VO < 50% can contribute to thermal storage, yet it should be appropriately controlled to avoid the influence of TCES thermal inertia. For a constant N operation, VO imposes little effect on thermal storage, so a smaller VO is preferable to increase the amount of thermal storage.

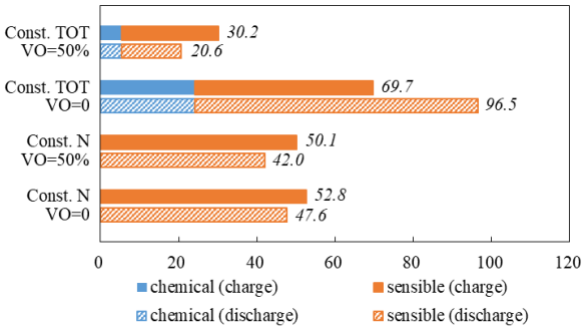

Fig. 15. Energy variations in TCES (kWh)

4.2.4.3 Overall performance and application

Critical operation parameters are listed in Table 4 to represent the overall performance of constant N and constant TOT strategies.

Because of the generally higher operating temperature in constant TOT operation, the total power generation and system efficiency was respectively 18 ~ 28 kWh and 2.0 ~ 3.4 percentage points higher than constant N operation for all bypass conditions. Thus, to obtain optimal power generation under a wide range of DNI variations, constant TOT operation is recommended. When a steady power supply voltage is critical, the system should switch to a constant N operation, in which case, the mass flow rate is highly steady while the operational ranges of $T_{rcv,out}$, and TIT are broadened.

Table 4. Overall performance of constant N and constant TOT operation

		Constant N	Constant TOT
Output power (kW_e)		0 ~ 13.1	0 ~ 14.8
Rotational speed (krpm)		120 ± 0.003	50 ~ 125
Mass flow rate (kg/s)		0.16 ~ 0.17	0.06 ~ 0.17
Receiver outlet temperature (K)		576 ~ 1147	754 ~ 1312
Turbine inlet temperature (K)		734 ~ 1149	944 ~ 1142
Turbine outlet temperature (K)		604 ~ 939	923 ± 1
Total electricity generation (kWh)	No-bypass	75.68	103.45
	Half-bypass	74.71	96.13
	Full-bypass	83.31	100.96

Thermoelectric conversion efficiency	No-bypass	10.88%	14.30%
	Half-bypass	10.74%	13.29%
	Full-bypass	11.97%	13.96%

5 Conclusions

To explore the operation and control strategies for a distributed solar-MGT-TCES system, a mathematical model was built and validated to analyze the system's thermodynamic characteristics under actual DNI conditions with both short- and long-term disturbances. Real-time control effects including performance stabilization and set point tracing are evaluated based on system dynamics. The results are listed below:

(1) Constant N operation can be achieved by power regulation when quickly and highly varying DNI is expected. With N and mass flow rate deviating less than 0.01% and 5.8%, respectively, the operation point is kept near the design point, and a stable power supply is available.

(2) Constant TOT operation can be achieved by power regulation through a cascade control. Optimal performance can be obtained, with TOT varying within 1 K and output power reaching 14.8 kW_e. The overall efficiency is also 2.0 ~ 3.4 percentage points greater than that of constant N operation, as the potentials of TCES is better exploited.

(3) Constant N-TOT simultaneous control can be accomplished by combining power and bypass regulations, generating a stable power of 12.6 kW_e ± 5% under 750 ~ 820 W/m^2 with a sharp drop to 500 W/m^2. Greater DNI_{tsh} and VO_0 values are recommended for clear and high-DNI weather conditions.

(4) The simulated cases provided evidence for a low risk of surging or choking of the operational strategies. TCES helps to stabilize system performance and prolongs generation time. It allows for constant TOT operation to store 32% (16.9 kWh) more energy than constant N and output 18 ~ 28 kWh more electricity during daytime operation.

In conclusion, the proposed real-time control strategies can provide stable, safe and efficient system operation, lessen the reliance on fossil fuel usage and facilitate the improvement of distributed high-percentage-solar-share MGT systems.

Future work includes the further improvement of control methods, such as multi-variable constrained control, as well as the experimentally realization of the control system.

Acknowledgements

The authors gratefully acknowledge the support from (1) National Natural Science Foundation of China (NO. 51776186), (2) Innovative Research Group Project of the National Natural Science Foundation of China (NO. 51621005) and (3) National Natural Science Foundation of China (NO. 51906214).

References

Achkari, O., Fadar, A.E., 2019. Latest developments on TES and CSP technologies - Energy and environmental issues, applications and research trends. Applied Thermal Engineering 167, 114806.

Albrecht, K.J., Ho, C.K., 2017. Heat Transfer Models of Moving Packed-Bed Particle-to-SCO 2 Heat Exchangers, ASME 2017 11th International Conference on Energy Sustainability.

Amelio, M., Pèrez, M.S., Ferraro, V., Rovense, F., Bova, S., 2018. Dynamic simulation of the temperature inlet turbine control system for an unfired micro gas turbine in a concentrating solar tower. Energy

Procedia.
Amsbeck, L., Buck, R., Heller, P., Jedamski, J., Uhlig, R., 2008. Development of a tube receiver for a solar-hybrid microturbine system, 14th Biennial CSP SolarPACES Symposium 2008.
Amsbeck, L., Denk, T., Ebert, M., Gertig, C., Rehn, J., 2010. Test of a Solar-Hybrid Microturbine System and Evaluation of Storage Deployment, SolarPACES 2010.
Azzouzi, D., Boumeddane, B., Abene, A., 2017. Experimental and analytical thermal analysis of cylindrical cavity receiver for solar dish. Renewable Energy.
Bittanti, S., Casamassima, V., Marco, A.D., Guagliardi, A., Karaj, B., 2013. A study for the control system of a hybrid solar-gas turbine power plant, 4th International Conference on Power Engineering, Energy and Electrical Drives. Istanbul, Turkey.
Buck, R., Giuliano, S., Uhlig, R., 2017. Central tower systems using the Brayton cycle. Advances in Concentrating Solar Thermal Research Technology, 353-382.
Carrillo, A.J., Moya, J., Bayón, A., Jana, P., de la Peña O'Shea, V.A., Romero, M., Gonzalez-Aguilar, J., Serrano, D.P., Pizarro, P., Coronado, J.M., 2014. Thermochemical energy storage at high temperature via redox cycles of Mn and Co oxides: Pure oxides versus mixed ones. Solar Energy Materials and Solar Cells 123, 47-57.
Cohen, H., Rogers, G.F.C., Straznicky, P., Saravanamuttoo, H.I.H., Nix, A., 1996. Gas Turbine Theory.
Criado, Y.A., Alonso, M., Abanades, J.C., Anxionnaz-Minvielle, Z., 2014. Conceptual process design of a CaO/Ca(OH)2 thermochemical energy storage system using fluidized bed reactors. Applied Thermal Engineering 73(1), 1087-1094.
CSIRO, 2014. Solar Air Turbine Project-Final report: project results.
Dixon, S.L., 2005. Fluid Mechanics and Thermodynamics of Turbomachinery, 5th ed. Pergamon Press.
Edwards, S.E.B., Materić, V., 2012. Calcium looping in solar power generation plants. Solar Energy 86(9), 2494-2503.
Ellingwood, K., Safdarnejad, S., Rashid, K., Powell, K., 2018. Leveraging Energy Storage in a Solar-Tower and Combined Cycle Hybrid Power Plant. Energies 12(1).
Ellingwood, K., Safdarnejad, S.M., Kovacs, H., Tuttle, J.F., Powell, K., 2019. Analysing the benefits of hybridisation and storage in a hybrid solar gas turbine plant. International Journal of Sustainable Energy(3), 1-29.
European Commission, 2005. SOLGATE-Solar Hybrid Gas Turbine Electric Power System.
European Commission, 2011. Solar-hybrid power and cogeneration plants.
Fallahi, A., Guldentops, G., Tao, M., Granados-Focil, S., Van Dessel, S., 2017. Review on solid-solid phase change materials for thermal energy storage: Molecular structure and thermal properties. Applied Thermal Engineering 127, 1427-1441.
Fisher, U., Sugarmen, C., Ring, A., Sinai, J., 2004. Gas Turbine "Solarization"-Modifications for Solar/Fuel Hybrid Operation. Journal of Solar Energy Engineering 126(3), 872.
Ghavami, M., Alzaili, J., Sayma, A.I., 2017. A Comparative Study of the Control Strategies for Pure Concentrated Solar Power Micro Gas Turbines, ASME Turbo Expo 2017: Turbomachinery Technical Conference and Exposition.
Gnielinski, V., 1976. New equations for heat mass transfer in turbulent pipe and channel flows.
Grange, B., Dalet, C., Falcoz, Q., Ferrière, A., Flamant, G., 2016. Impact of thermal energy storage integration on the performance of a hybrid solar gas-turbine power plant. Applied Thermal Engineering.
Guédez, R., Spelling, J., Laumert, B., 2013. Thermoeconomic Optimization of Solar Thermal Power

Plants with Storage in High-penetration Renewable Electricity Markets, ISES Solar World Congress.
Haugwitz, S., 2003. Modelling of Microturbine Systems. European Control Conference.
Heller, P., Jedamski, J., Amsbeck, L., Uhlig, R., Ebert, M., Svensson, M., Denk, T., Hilgert, C., Fisher, U., Sinai, J., Gertig, C., Tochon, P., 2009. Development of a Solar-Hybrid Microturbine System for a Mini-Tower, SolarPACES.
Heller, P., Pfänder, M., Denk, T., Tellez, F., Valverde, A., Fernandez, J., Ring, A., 2006. Test and evaluation of a solar powered gas turbine system. Solar Energy.
Henke, M., Monz, T., Aigner, M., 2017. Introduction of a New Numerical Simulation Tool to Analyze Micro Gas Turbine Cycle Dynamics. Journal of Engineering for Gas Turbines Power.
Hiromi, N., Toshiyuki, O., Kazuta, K., Masaharu, W., Masashi, T., 2012. Development of Concentrated Solar Power Generation System with Hot Air Turbine. Mitsubishi Heavy Industries Technical Review 49.
Hohloch, M., Zanger, J., Widenhorn, A., Aigner, M., 2010. Experimental Characterization of a Micro Gas Turbine Test Rig, ASME Turbo Expo 2010: Power for Land, Sea & Air. Glasgow, UK, pp. 671-681.
Korzynietz, R., Brioso, J.A., del Río, A., Quero, M., Gallas, M., Uhlig, R., Ebert, M., Buck, R., Teraji, D., 2016. Solugas - Comprehensive analysis of the solar hybrid Brayton plant. Solar Energy.
Korzynietz, R., Quero, M., Uhlig, R., 2012. SOLUGAS-future solar hybrid technology, SolarPACES.
Lanchi, M., Montecchi, M., Crescenzi, T., Mele, D., Miliozzi, A., Russo, V., Mazzei, D., Misceo, M., Falchetta, M., Mancini, R., 2015. Investigation into the Coupling of Micro Gas Turbines with CSP Technology: OMSoP Project. Energy Procedia Volume 69, Pages 1317-1326.
Llamas, J.M., Bullejos, D., Adana, M.R.d., 2019. Optimal Operation Strategies into Deregulated Markets for 50 MWe Parabolic Trough Solar Thermal Power Plants with Thermal Storage. Energies.
Lovegrove, K., Luzzi, A., Soldiani, I., Kreetz, H., 2004. Developing ammonia based thermochemical energy storage for dish power plants. Solar Energy 76(1-3), 331-337.
Merchan, R.P., Santos, M.J., Medina, A., Calvo Hernandez, A., 2017. Thermodynamic model of a hybrid Brayton thermosolar plant. Renewable Energy 128(PT.B), 473-483.
Olivenza-León, D., Medina, A., Calvo Hernández, A., 2015. Thermodynamic modeling of a hybrid solar gas-turbine power plant. Energy Conversion and Management 93, 435-447.
Quero, M., Korzynietz, R., Ebert, M., Jiménez, A.A., del Río, A., Brioso, J.A., 2014. Solugas – Operation Experience of the First Solar Hybrid Gas Turbine System at MW Scale. Energy Procedia 49(2014), 1820-1830.
Rovense, F., 2015. A Case of Study of a Concentrating Solar Power Plant with Unfired Joule-Brayton Cycle. Energy Procedia 82, 978-985.
Rovense, F., Amelio, M., Ferraro, V., Scornaienchi, N.M., 2016. Analysis of a Concentrating Solar Power Tower Operating with a Closed Joule Brayton Cycle and Thermal Storage. International Journal of Heat Technology 34(3).
Rovense, F., Amelio, M., Scornaienchi, N.M., Ferraro, V., 2017. Performance analysis of a solar-only gas micro turbine, with mass flow control. Energy Procedia 126, 675-682.
Rovense, F., Reyes-Belmonte, M.A., Gonzalez-Aguilar, J., Amelio, M., Bova, S., Romero, M., 2019. Flexible electricity dispatch for CSP plant using un-fired closed air Brayton cycle with particles based thermal energy storage system. Energy 173(APR.15), 971-984.
Schwarzboezl, P., Buck, R., Sugarmen, C., Ring, A., Crespo, M.J.M., Altwegg, P., Enrile, J., 2006. Solar gas turbine systems: Design, cost and perspectives. Solar Energy 80(10), 1231-1240.

Sinai, J., Sugarmen, C., Fisher, U., 2005. Adaptation and Modification of Gas Turbines for Solar Energy Applications, ASME Turbo Expo 2005: Power for Land, Sea, and Air. Reno, Nevada, USA.

Singh, A., Tescari, S., Lantin, G., Agrafiotis, C., Roeb, M., Sattler, C., 2017. Solar thermochemical heat storage via the Co3O4/CoO looping cycle: Storage reactor modelling and experimental validation. Solar Energy.

Spelling, J., Guédez, R., Laumert, B., 2014. A Thermo-Economic Study of Storage Integration in Hybrid Solar Gas-Turbine Power Plants. Journal of Solar Energy Engineering.

Spelling, J., Laumert, B., 2014. Thermoeconomic Evaluation of Solar Thermal and Photovoltaic Hybridization Options for Combined-Cycle Power Plants. Journal of Engineering for Gas Turbines Power 137(3), 031801.

Ssebabi, B., Dinter, F., Johan, v.d.S., Schatz, M., 2019. Predicting the performance of a micro gas turbine under solar-hybrid operation. Energy Conversion and Management 177(JUN.15), 121-135.

Tescari, S., Agrafiotis, C., Breuer, S., De Oliveira, L., Puttkamer, N.V., Roeb, M., Sattler, C., 2014. Thermochemical solar energy storage via redox oxides: materials and reactor/heat exchanger concepts. Energy Procedia 49.

Tescari, S., Lantin, G., Lange, M., Breuer, S., Agrafiotis, C., Roeb, M., Sattler, C., 2015. Numerical model to design a thermochemical storage system for solar power plant. Energy Procedia.

Tian, Y., Zhao, C.Y., 2013. A review of solar collectors and thermal energy storage in solar thermal applications. Applied Energy 104, 538-553.

Traverso, A., 2004. TRANSEO: A New Simulation Tool For Transient Analysis Of Innovative Energy Systems, DIMSET. Università di Genova, Italy.

Traverso, A., Barberis, S., Lima, D., Massardo, A.F., 2014. Dynamic Analysis of Concentrated Solar Hybridised Gas Turbine, ASME Turbo Expo 2014: Turbine Technical Conference and Exposition.

Wacek, E., Ferguson, W., Application of the latest aeroderivative gas turbine technology. General Electric, 09-IAGT 203.

Wang, W., Malmquist, A., Laumert, B., 2018. Comparison of potential control strategies for an impinging receiver based dish-Brayton system when the solar irradiation exceeds its design value. Energy Conversion Management.

Xu, B., Li, P., Chan, C., 2015. Application of phase change materials for thermal energy storage in concentrated solar thermal power plants: A review to recent developments. Applied Energy 160(DEC.15), 286-307.

Yang, G., Xiao, G., Yang, T., Ni, M., Cen, K., 2017. Thermal Kinetics of CuO/Cu2O redox system. SolarPaces.

Zalba, B., Marín, J.M., Cabeza, L.F., Mehling, H., 2003. Review on thermal energy storage with phase change: materials, heat transfer analysis and applications. Applied Thermal Engineering 23(3), 251-283.

Zhou, X., Mahmood, M., Chen, J., Yang, T., Ferrari, M.L., 2019. Validated model of thermochemical energy storage based on cobalt oxides. Applied Thermal Engineering 159, 113965-.

Nomenclature

Abbreviations

CSP	Concentrated solar power
DNI	Direct normal irradiance, W/m^2

HSA	High speed alternator
INV	Inverter
LCOE	Levelized cost of energy
MGT	Micro gas turbine
PI	Proportion Integration
PID	Proportion Integration Differentiation
REC	Rectifier
TES	Thermal energy storage
TCES	Thermochemical energy storage
TIT	Turbine inlet temperature, K
TOT	Turbine outlet temperature, K
VO	Valve opening, %

Greek Symbols

γ	Specific heat ratio
ε	Emissivity
η	Efficiency
π	Circular constant
ρ	Density, kg/m^3
σ	Stefan-Boltzmann constant, W/(m^2·K^4)
ω	Rotational speed, rad/s

Roman Symbols

A	Area, m^2
A_d	Differentiation gain
C_p	Constant pressure heat capacity, J/(kg·K)
C_t	Reactant concentration, mol
C_v	Constant volume heat capacity, J/(kg·K)
CO_2	Carbon dioxide
Co_3O_4	Cobalt oxide
CoO	Cobaltous oxide
ER	Expansion ratio
ΔH_r	Reaction enthalpy, J/mol
h	Heat transfer coefficient, W/(m^2·K)
J	Rotational mechanical inertia, kg·m^2
K_c	Proportion gain
K_i	Integration constant

K_p	Proportion constant
L	Length, m
M	Mass, kg
$\dot{m}$	Mass flow rate, kg/s
N	Rotational speed, rpm
O_2	Oxygen
P	Pressure, Pa
PR	Pressure ratio
PW	Power, W
$\dot{Q}$	Energy flux, W
R_g	Gas constant, J/(mol·K)
R_t	Reaction rate, s^{-1}
$\dot{S}_h$	Chemical reaction energy, W
T	Temperature, K
T_i	Integration time
T_d	Differentiation time
t	Time, s
U	Overall heat transfer coefficient, $W/(m^2 \cdot K)$
V	Volume, m^3

Subscripts

ac	Convective heat loss through aperture
air	Air
amb	Ambient
ar	Radiative heat loss through aperture
c	Compressor; cold side of recuperator
chem	Chemical heat
chr	Charging state
conv	Convective heat transfer
corrected	Corrected variable
disc	Discharging state
field	Heliostat field
gt	Gas turbine
h	Hot side of recuperator
in	Inlet
icav	Internal cavity
load	Load power

loss	Heat or pressure loss
M	Metal bulk
m	Mean value of flow
max	Maximum
min	Minimum
mir	Heliostat mirror
net	Net power
out	Outlet
r	Heat loss through radial direction
rcv, out	Receiver outlet
ref	Reference
sen	Sensible heat
set	Set point
sim	Simulation
t	Turbine
tsh	Threshold
use	Useful part
wicav	Wall of inner cavity
z	Heat loss through bottom direction
0	Original value
01	Compressor inlet
02	Compressor outlet
06	Turbine inlet
07	Turbine outlet

Appendix: Model validation

A. Receiver

The receiver validation experiment was conducted in the solar tower test rig in Zhejiang University in China (Fig. 16), with one hundred 4 m-by-5 m heliostats and a 1.5 m-wide circular aperture located at the height of 35 m. The experiment started at 9:41 AM on Sep. 23rd, 2019, corresponding to time 0 at Fig. 17. The ambient air was driven by an air compressor and entered the receiver. Meanwhile, heliostats focused on the receiver aperture group after group (Fig. 17 (a)) to avoid excessive heating rate which is harmful to the materials of receiver and the protection board in its surrounding. Fig. 17 (b) presents the response of receiver outlet temperature under DNI fluctuation and mass flow rate step-change. The pressure of the hot air is the ambient pressure.

Fig. 16. Solar tower test rig at Zhejiang University, China

Table 5. Receiver parameters

Parameter	Value	Parameter	Value
Aperture diameter	0.5 m	Tube inner diameter	9.22 mm
Receiver outer diameter	0.86 m	Tube thickness	2.24 mm
Receiver length	1.24 m	Tube length	0.97 m
Insulation thickness	0.2 m	Insulation material	Aluminum silicate fiber felt
Number of tubes in total	60*2	Tube material	Inconel 625

Note: For better understanding of the structural parameters, please refer to Fig. 2.

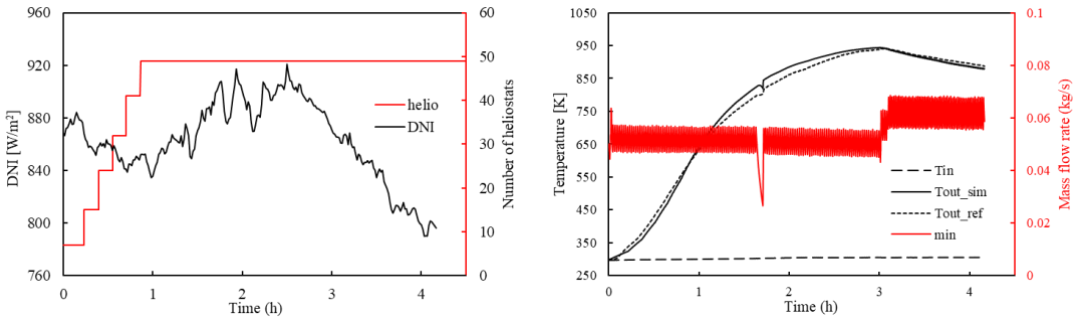

(a) DNI and heliostat number variations (b) Temperature and mass flow rate variations

Fig. 17. Receiver model validation against in-house test data

B. TCES

The TCES model validation is conducted against DLR's test data (Singh et al., 2017), as shown in Fig. 18. The solid temperature in the top and middle positions as well as the outlet air temperature are compared. The maximum deviations are summarized in Table 2. The top and middle solid temperatures show larger discrepancies than the outlet air temperature. For the top solid temperature, the gap mainly happens in steady phase when the heat transfer in the top layer has reached the equilibrium. The deviation is mainly caused by the thermal loss calculation. For the middle solid temperature, the gap mainly happens in the rising and falling phases after reduction and oxidation complete, respectively. This type of deviation is mostly caused by the redox reaction kinetics calculation, involving the reaction rate, conversion ratio, etc.

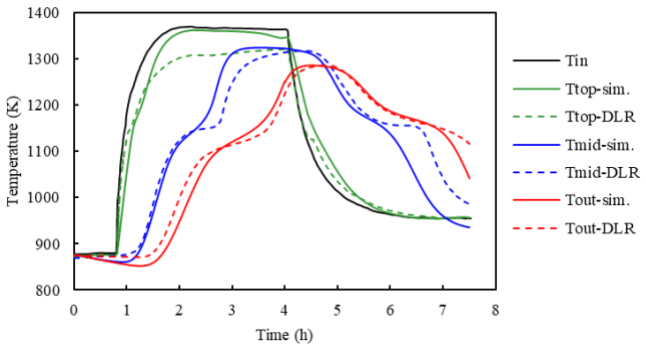

Fig. 18. TCES model validation against DLR test (Singh et al., 2017)